Numerical simulation of fast ion loss detector measurements for fishbones on JET

Numerical simulation of fast ion loss detector measurements for fishbones on JET

C. Perez von Thun[1]**, A. Perona**[2]**, T. Johnson**[3]**, M. Reich**[1]**,
S.E. Sharapov**[4]**, V.G. Kiptily**[4]**, M. Cecconello**[5]**, A. Salmi**[6]**,
V.Ya. Goloborod'ko**[7]**, S.D. Pinches**[4]**, M. García-Muñoz**[1]**,
D. Darrow**[8]**, M. Brix**[4]**, I. Voitsekhovitch**[4] **and JET EFDA
contributors**[a]

JET-EFDA Culham Science Centre OX14 3DB, Abingdon, UK
[1] Max-Planck-Institut für Plasmaphysik, EURATOM-Association IPP, Garching, D-85748, Germany
[2] Burning Plasma Research Group, Politecnico di Torino, 10129 Torino, Italy
[3] EURATOM-VR Association, Fusion Plasma Physics, EES, KTH, 10044 Stockholm, Sweden
[4] EURATOM/CCFE Fusion Association, Culham Science Centre, Abingdon, OX14 3DB, UK
[5] EURATOM-VR Association, Department of Physics and Astronomy, Uppsala University, 75120 Uppsala, Sweden
[6] Helsinki University of Technology, Association EURATOM-Tekes, Helsinki, Finland
[7] Association EURATOM/OEAW, Institute for Theoretical Physics, University of Innsbruck, Innsbruck, Austria
[8] Princeton Plasma Physics Laboratory, Princeton, NJ, USA

E-mail: Christian.Perez.Von.Thun@jet.efda.org

Abstract

A synthetic diagnostic model for the simulation of energy and pitch angle resolved measurements of fast ion losses obtained by 2D scintillation-type detectors is presented and subsequently tested on a JET discharge with fishbones (previously documented in Perez von Thun *et al* 2010 *Nucl. Fusion* **50** 084009). The simulated energy and pitch angle distributions at the detector are found to be in excellent agreement with the measurements. The simulations further suggest that nearly all the fast ion losses take place in the early growth phase of the fishbone cycle, and reach their maximum well ahead of the magnetic perturbation peak.

(Some figures in this article are in colour only in the electronic version)

1. Introduction

To achieve ignition (or a high fusion energy gain) in a D–T operated magnetic confinement fusion device and prevent damage to plasma facing wall elements [1], it is necessary that the fast (i.e. suprathermal) ions generated through auxiliary heating and fusion born alpha particles remain confined until they transfer their energy to the plasma. Electromagnetic field perturbations generated by the presence of instabilities in the plasma can lead to a premature loss of the fast alphas, either through resonant or non-resonant wave–particle interaction

processes [2, 3]. In tokamaks one such type of instability is fishbone oscillations [4, 5]. Fishbones are commonly observed at low (sub-Alfvénic) frequencies and driven unstable by the presence of a fast ion population in the plasma which interacts with the internal kink mode. Resonant fishbone losses are considered of less concern for burning plasmas, because they are predicted to involve only relatively low energy (few hundred keV) alphas [6] (at higher energies the characteristic frequencies associated with the alpha periodic motion, i.e. the poloidal and toroidal transit times, are such that it becomes difficult to enter resonance with a low frequency wave). However, in [6] it was also pointed out that non-resonant losses of fusion products by fishbones may become an issue, as they could also affect the higher energy part of

---

[a] See the appendix of F. Romanelli *et al* 2008 *Proc. 22nd IAEA Fusion Energy Conf. (Geneva, Switzerland, 2008).* http://www.naweb.iaea.org/napc/physics/FEC/FEC2008/papers/ov_1-2.pdf
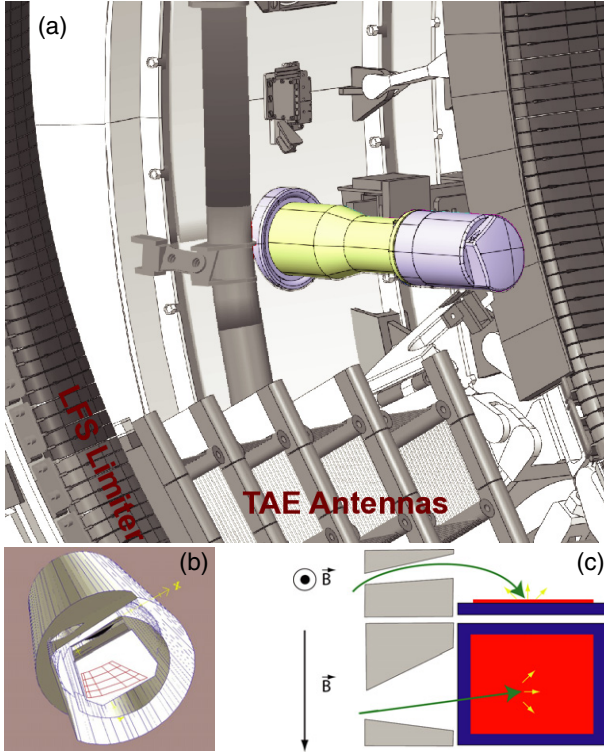
Figure 1. (*a*) Scintillator probe layout inside the JET vessel. (*b*) Cross-cut through the probe head showing the collimator and the 2D scintillator plate. (*c*) Measuring principle: the location at which incoming ions hit the scintillator depends on the gyroradius and the pitch angle of the velocity vector with respect to the local magnetic field.

Figure 2. Waveform of the $n = 1$ kink amplitude used in HAGIS, including the definitions of the quantities t_{sat}, t_{period} and A_{sat}. $A \equiv \delta \tilde{B}_r / B_0$ is the perturbed radial magnetic field normalized to the magnetic field on axis.

the fast alpha population. These fast ion losses are predicted to arise due to the loss of toroidal symmetry of the magnetic field configuration (and hence of the loss of constancy of the canonical momentum, P_ϕ) in the presence of the mode. Indeed, increased fusion product losses in the MeV range have been reported on a number of machines in the presence of fishbones, including JET [7–10]. In the case of [10], the losses were characterized with the help of a 2D scintillator diagnostic for lost ions [11], shown in figure 1, assessing in particular the energy and pitch angle distribution of the losses, their scaling with the fishbone amplitude as well as the losses' temporal evolution during a fishbone cycle. Also in [10], results from numerical simulations were presented which, using a number of simplifying assumptions, aimed at reproducing the experimental measurements. The simulation results were mostly in broad agreement with experiment, but some of the predictions could not be reconciled with experiment using this model. This paper is a continuation of that work. The key improvement compared with [10] is the more accurate geometric selection of losses reaching the scintillator with the help of a synthetic diagnostic model for the scintillator probe which has been developed and incorporated into the HAGIS (v10.04) orbit following code, and which replicates better the actual working principle of the diagnostic. Also compared with [10], a more accurate treatment of the instrumental function of the scintillator diagnostic has been implemented. The paper is structured as follows. Section 2 presents the numerical model used, with emphasis on the synthetic diagnostic module which
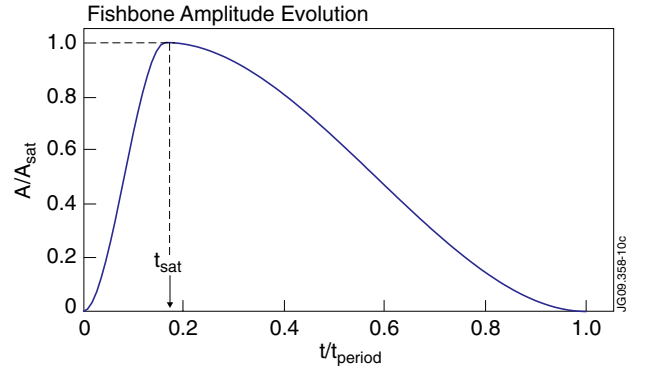
replicates the scintillator probe inside HAGIS. In section 3 this model is applied to a test case discharge and the outcome compared with experiment. In the final section a summary of results is provided, the conclusions are drawn and an outlook for future work is given.

2. Numerical model

A time-dependent 3D magnetic configuration is constructed by superimposing the perturbation field of an internal kink mode (whose radial eigenfunction is a good approximation for the fishbone) to the axisymmetric equilibrium. Here, the radial eigenfunctions are computed by the linear MHD code MISHKA-1, which solves the ideal incompressible MHD equations. To reproduce a typical fishbone cycle, the obtained eigenfunctions are scaled analytically with a time-dependent amplitude and rotation frequency. The amplitude is specified through a third order polynomial as follows. For $t \leqslant t_{sat}$

$$\frac{A(t)}{A_{sat}} = \frac{t^2}{t_{sat}^3}(3t_{sat} - 2t) \tag{1}$$

whereas for $t_{sat} < t \leqslant t_{period}$:

$$\frac{A(t)}{A_{sat}} = (t_{period} - t)^2 \frac{[3(t_{period} - t_{sat}) - 2(t_{period} - t)]}{(t_{period} - t_{sat})^3} \tag{2}$$

where $A \equiv \delta \tilde{B}_r / B_0$ is the radial perturbation amplitude (normalized to the magnetic field on axis), t_{sat} is the time at which the maximum fishbone amplitude, A_{sat}, is reached, and t_{period} is the total duration of the fishbone. The waveform appearance is illustrated in figure 2. The perturbation frequency is chosen to decrease linearly in time over the fishbone period.

From the above discussion it becomes clear that non-linear effects are only empirically included through the prescribed amplitude and frequency evolution, whereas non-linear modifications to the radial eigenfunction are not considered here. Non-linear MHD effects on fishbones have been studied numerically and analytically in [12], using a non-linear reduced MHD model [13, 14] combined with a linear response for the energetic particles. It was found that when the energetic particle pressure is close to the instability
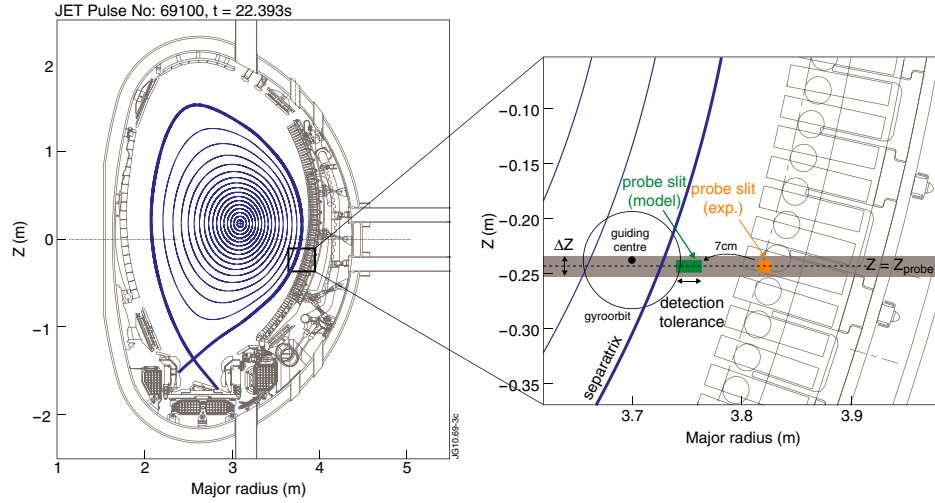
Figure 3. Synthetic diagnostic model used in HAGIS to select scintillator probe detected ions.

threshold, the top-hat linear eigenmode profile splits up into a two-step structure around the $q = 1$ flux surface (typically, the radial distance between steps remains small compared with the $q = 1$ radius), whereas well above the instability threshold the two steps merge into a single layer, yielding a mode similar to the ideal $n = 1$ kink instability. In both cases the eigenfunction does not strongly depart from the ideal $n = 1$ kink eigenfunction, so our eigenfunction approximation appears to be justified even for large fishbones. However, one needs to bear in mind that the linear approach may still become unsuitable if the amplitudes involved are sufficiently high to change the magnetic topology of the equilibrium configuration. For the example discharge treated here the threshold for magnetic field line stochastization is found to lie near $A = 1.75 \times 10^{-2}$, so for the simulation results shown here we will limit ourselves to lower values of the fishbone saturation amplitude.

The drift-orbit following code HAGIS [15, 16] follows an ensemble of fast particles in the time-dependent magnetic field configuration throughout the duration of a fishbone cycle, where the initial fast particle ensemble is computed externally by a Fokker–Planck Monte Carlo solver (for the example presented in section 3 this code is SELFO). In order to simulate the scintillator probe measurements, a synthetic diagnostic model has been added to HAGIS, whose layout is shown in figure 3. Each time a guiding centre crosses a pre-defined horizontal plane $Z = Z_{\mathrm{probe}}$, HAGIS computes the ion's Larmor radius and checks by how much the guiding centre distance to the probe entrance slit (centred at R_{probe}, Z_{probe}) deviates from the Larmor radius. If this deviation is less than a given tolerance value (this value determines the effective radial width of the probe slit in the simulation), the ion is pre-selected. In reality, the actual width of the probe slit is 0.6 mm, but the tolerance value used here was set to 1 cm in order to improve the simulation statistics (this artefact is equivalent to, but cheaper than, increasing the number of particles). For the same reason, in the model the probe slit is chosen to be not toroidally localized (so we assume toroidal symmetry of the losses), whereas in reality the toroidal extension of the probe slit is a few mm only. Furthermore, it is ensured that each ion can be detected only once (recurrent detections

are ignored). In practice some of the ions would have been detected also in the absence of a perturbation. These ions are discarded through comparison with a reference simulation for which the perturbation field has been switched off. The collimator of the real scintillator probe is designed in such a way that only ions whose gyroradius and pitch angle lie within a certain range (3–13 cm and 35–85°, respectively) can actually hit the scintillator plate, so ions which fall outside this range are discarded in the synthetic diagnostic. For a successful detection the ions also need to reach the slit within an allowable range of gyrophases (the incidence angle must not deviate by more than approximately 25° from the slit plane normal). This is ensured by requesting that the guiding centre does not deviate by more than $\Delta Z/2$ from Z_{probe} for detection (shaded area in figure 3). In practice, ΔZ is not an explicit parameter, but its value has been fixed indirectly by adjusting the numerical stepsize when computing the orbit trajectory. Here, the value of $\Delta Z/2$ was approximately 1 cm.

An important approximation that had to be made concerns the probe location. In the experiment setup, the probe entry slit is located at $R = 3.821$ m, $Z = -0.242$ m. As for the discharge analysed here the distance from the probe slit to the plasma boundary is more than a gyroradius, and since with the HAGIS version available for our studies it was not possible to compute drift orbit trajectories beyond the separatrix, it became necessary to shift in our modelling the probe position radially inwards by 7 cm to $R = 3.751$ m (this is the smallest possible displacement that still guarantees that all the measurable ions—i.e. with gyroradius of at least 3 cm—can be detected). The impact of this artificial shift on our simulation results will be discussed later in more detail. This approach is only acceptable if the probe measurements are not affected by shadowing effects from nearby wall components (the most notable candidates being a poloidal limiter and a toroidal Alfvén eigenmode excitation antenna, both of which are depicted in figure 1(*a*)), as otherwise moving the probe position radially could dramatically change the results. Separate full orbit following simulations have been carried out using a Monte Carlo code [17]—which includes a 3D model of the JET wall—in which particles were started at the scintillator probe entrance slit and traced backwards in time. The energy
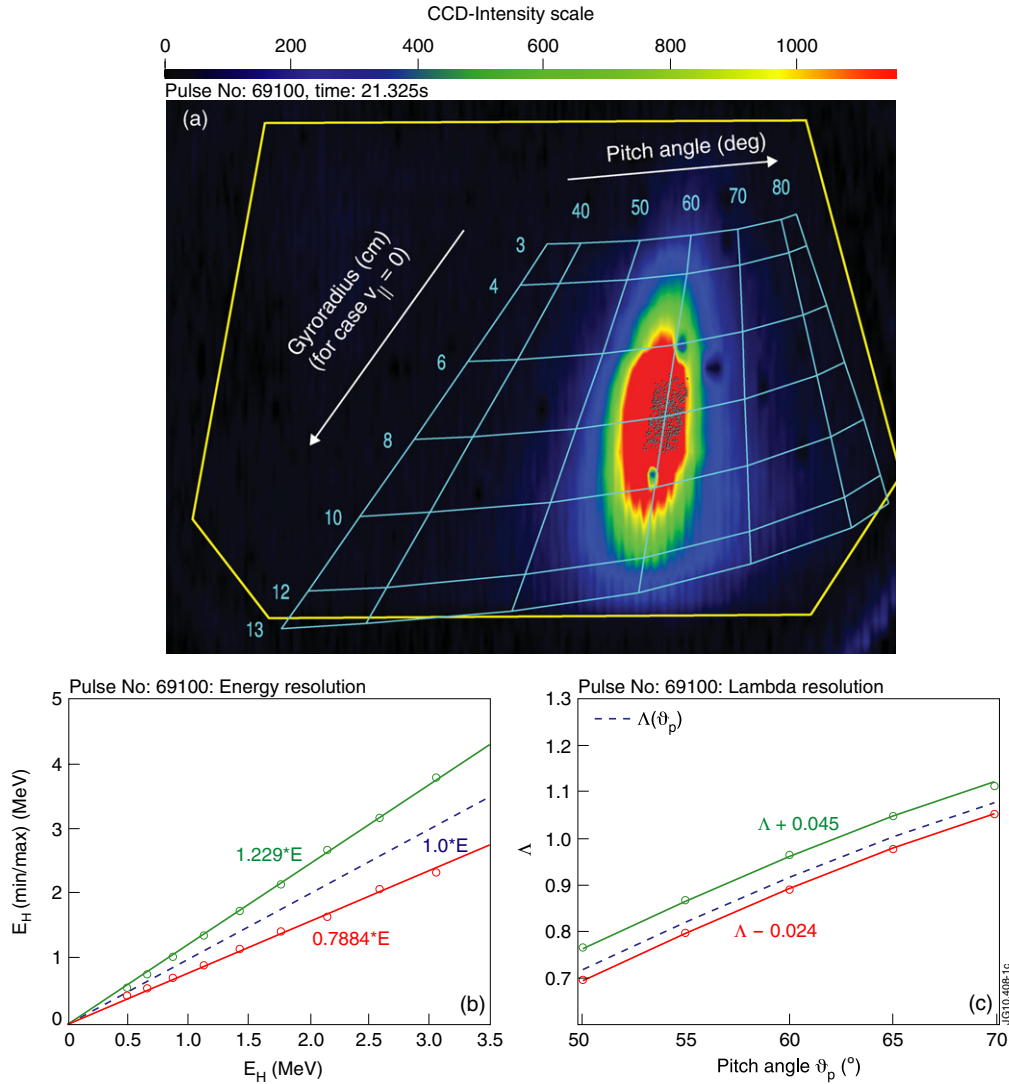
Figure 4. Determination of the instrumental function of the diagnostic for discharge 69100: (*a*) snapshot of the 2D scintillator plate emission, where the colour scale increases with the increasing light output. Superimposed is a grid with the gyroradii and pitch angle coordinates of the detected ions. Also shown is an ensemble of black dots, forming an approximate rectangle, which have been generated by the efipdesign orbit following Monte Carlo code to compute the instrument resolution (see text). In the example shown particles have been started randomly at the collimator entrance with a gyroradius of 8 cm and a pitch angle of $60°$ and followed until they hit the scintillator plate. (*b*) Obtained energy resolution of the diagnostic (minimum and maximum energy bounds) versus energy (here for protons and including a correction for the gold foil filter) and their linear fit. (*c*) Obtained Λ resolution of the diagnostic, yielding an essentially constant resolution across the entire range of pitch angles.

and pitch values of the launched test ions were scanned in order to cover the full range measurable by the diagnostic. It was found that for the discharge considered in this paper shadowing effects are indeed not present. The TAE antenna does not capture any of the ions because the *B*-field pitch is too low, whereas the high plasma triangularity moves the ions away from the limiter.

It is finally noted that this geometric description is much more sophisticated than the one used previously in [10]. There, the criterion used for selection was that guiding centres had to cross the separatrix within a range of poloidal angles in the vicinity of the probe, i.e. $-60° < \theta < 0°$ with respect to the plasma midplane. That is a relatively rough approximation in that this area is poloidally extended and the details of the gyromotion (e.g. gyrophase at probe slit) are not taken into account, hence many of the ions satisfying that criterion were in

reality still not detectable. These deficiencies are now resolved with the new model, which replicates the actual working principle of the scintillator diagnostic in a more realistic way.

In order to be able to compare the output from HAGIS with the experimental measurement, the instrumental function of the scintillator diagnostic has to be known. The instrumental function is magnetic configuration dependent and hence has to be computed on a case by case basis. This has been determined outside HAGIS with the help of a Monte Carlo tool ('efipdesign') [11, 18] that for a given gyroradius and pitch angle pair of values initializes particles at random positions and gyrophases on the entrance slit, follows their trajectories through the collimator towards the scintillator plate and records their strike points. One example run is shown in figure 4(*a*). Within the gyroradius and pitch angle resolution of the diagnostic, the distribution of strikes is almost flat and

hence the instrumental function can be well approximated by a step function. The resolution itself is gyroradius and pitch angle dependent. It is computed by carrying out this procedure for an ensemble of gyroradii and pitch angles and fitting the result. As for the HAGIS simulations output we will be using the constants of motion quantities E and $\Lambda = \mu_{\mathrm{m}} B_0/E = B_0(1 - \cos^2 \vartheta_{\mathrm{p}})/B$ (where μ_{m} is the magnetic moment, E is the proton energy, B_0 and B are the magnetic fields on axis and at the probe location, respectively, and ϑ_{p} is the pitch angle), rather than the gyroradius and pitch angle, the instrument resolution is computed in terms of these quantities. The resulting fit for the case of JET discharge 69100 is shown in figures 4(*b*) and (*c*). As a further improvement to the analysis performed in [10], rather than classifying the output distribution from HAGIS into energy and pitch angle (or Λ) bins set by the instrument resolution, the output distribution is now directly convoluted with the instrumental function on a particle by particle basis, which, as will be shown, yields smoother and more accurate results.

Another important aspect of the diagnostic is the scintillator material itself (P56 or $Y_2O_3 : Eu^{3+}$), which has a relatively long phosphorescence decay time of 2 ms. This may lead to distortions of the overall light output behaviour for fast events which, however, would not show up on the energy and pitch angle distribution measurements [19, 20]. Note that this phosphorescence time affects only the light decay, the rise time is not affected and can be much faster. So here the temporal instrument function will be simply approximated by

$$I(t) \sim \begin{cases} 0 & (t < t_{\mathrm{detect}}) \\ \mathrm{e}^{-500*(t-t_{\mathrm{detect}})} & (t \geqslant t_{\mathrm{detect}}). \end{cases}$$

3. Application to JET discharge

We have repeated an earlier analysis done for JET discharge 69100, documented in detail in [10], with the improved numerical model. A brief review of the discharge characteristics and main experimental findings is given here for convenience.

Discharge 69100 is an ELMy H-mode discharge with conventional (fully relaxed) q-profile. During its flat top ($t = 21.0$–23.4 s) the discharge parameters are as follows: $B_0 = 2.7$ T, $I_{\mathrm{p}} = 1.2$ MA, edge safety factor $q_{95} \sim 6.5$, normalized beta $\beta_{\mathrm{N}} = 2.6$, poloidal beta $\beta_{\mathrm{pol}} = 1.8$, Greenwald fraction $n_{\mathrm{e}}/n_{\mathrm{GW}} = 0.77$, triangularity $\delta \sim 0.4$. The plasma is composed of 95% deuterium and 5% hydrogen (inferred from visible spectroscopy measurements at the plasma boundary). The auxiliary heating consists of 15 MW of NBI (deuterium, max. 130 keV injection energy) and 6 MW of coupled ICRH (42 MHz, giving for the hydrogen minority a central resonance position 28 cm inboard of the magnetic axis). The neutral particle analyser (NPA) diagnostics show negligible second harmonic deuterium acceleration, which is in agreement with PION [21] and SELFO [22] simulations. Fishbone bursts are repeatedly observed throughout the flattop phase. Their occurrence is accompanied by a temporary increase in fast ion losses detected by the scintillator probe (figure 5). Neutron emission traces and also ICRH-free reference discharges demonstrate that the fishbones are driven unstable by neutral beam injected deuterons. However, any

neutral beam deuterons lost from the plasma (e.g. due to resonant interaction with the fishbone wave field) will not be detected by the scintillator diagnostic as deuterons with $E_{\mathrm{D}} < 200$ keV are blocked by a gold foil with 1 μm thickness mounted at the probe entrance. Instead, the fast ion losses seen on the scintillator probe are identified as ICRH-accelerated protons in the megaelectronvolt energy range, which become lost due to non-resonant wave–particle interaction [10].

For the simulations, the proton distribution of ICRH-accelerated protons in the plasma has been computed with the SELFO code for this discharge. The resulting distribution has been validated against NPA measurements by comparing the perpendicular tail temperature (mean energy in the perpendicular degrees of freedom) of the simulated distribution along the NPA's line of sight with the actual NPA measurement. Within the measurement uncertainty, excellent agreement is found between the two tail temperatures (249 keV by SELFO, 240 ± 65 keV by NPA).

The magnetic perturbation field computed by MISHKA (internal kink mode including poloidal harmonics $-2 \leqslant m \leqslant +4$) is superimposed onto the 2D equilibrium using the following parameters: $t_{\mathrm{sat}} = 1.8$ ms, $t_{\mathrm{period}} = 11.0$ ms, $f_{\mathrm{start}} = 7$ kHz, $f_{\mathrm{end}} = 2$ kHz, whereas A_{sat} has been varied between 0.25×10^{-2} and 1.50×10^{-2} to cover the full range of fishbone amplitude values observed in discharge 69100. Here, the first two parameters have been inferred directly from magnetic fluctuation traces, the third and fourth parameters are the fishbone oscillation frequencies after deduction of the core plasma rotation near the $q = 1$ rational surface (from charge exchange recombination spectroscopy). Finally, the value of $A_{\mathrm{sat}} = \delta \tilde{B}_{r,\mathrm{sat}}/B_0$ has been obtained by matching the magnitude of magnetic flux surface displacements inside $q = 1$ (visualized through Poincaré plots of magnetic field lines in the 3D perturbed equilibrium) to electron temperature profile displacements at the time of maximum fishbone amplitude measured with an array of ECE radiometers. The electron temperature profile displacements are in turn obtained using the expression

$$\xi = \frac{\delta T_{\mathrm{e}}}{|\nabla T_{\mathrm{e}}|}, \tag{3}$$

which neglects plasma compressibility [23]. It is noted that the distortion of the total magnetic field (ECE measurement position) as a result of the fishbone perturbation is negligible, and that the plasma is optically thick at the location of interest, so the ECE signal responds indeed only to electron temperature variations.

The simulation results are as follows. As in the earlier simulations (cf also [10, figures 12 and 13]), two orbit types are the main contributors to the detected losses: (*a*) trapped protons whose outer orbit leg runs close to the plasma boundary (and thus were already passing by in the vicinity of scintillator diagnostic), and (*b*) from counter-passing protons deep inside the plasma which transit into a trapped orbit similar to (*a*). In both cases the orbit distortions are found to originate from non-resonant wave–particle interaction. Figure 6(*a*) shows the energy distribution of detected protons predicted by HAGIS for discharge 69100 for a fishbone with amplitude $A_{\mathrm{sat}} = 1.0 \times 10^{-2}$. This distribution is subsequently convoluted with the instrumental function of the scintillator and normalized to yield the measurement prediction shown in figure 6(*b*),
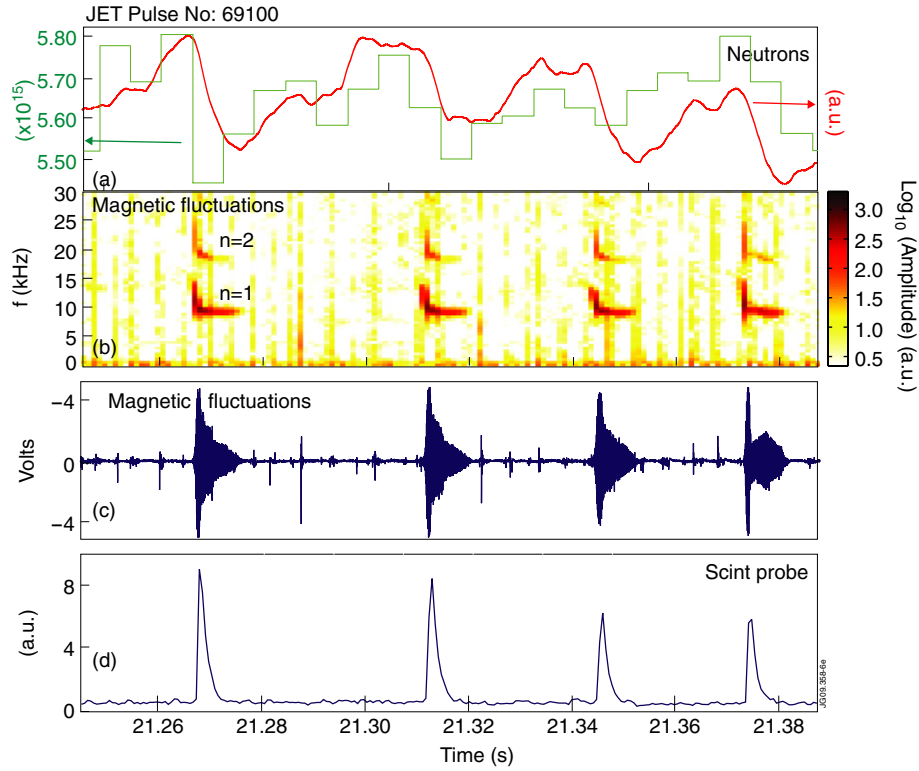
Figure 5. Time interval of discharge 69100 with four fishbones. (*a*) Neutron emission (two traces are shown: a slow calibrated signal and a faster signal which is uncalibrated), (*b*) magnetic fluctuation spectrogram (and toroidal mode numbers *n* measured by a toroidal array of coils). The fishbones are visible in the frequency range 9–14 kHz, and a fishbone harmonic at twice that frequency. The mode is further detected by an array of ECE channels deep in the plasma core. (*c*) Magnetic fluctuation time trace (the much smaller bursts visible on this trace are due to ELMs), (*d*) scintillator probe signal.
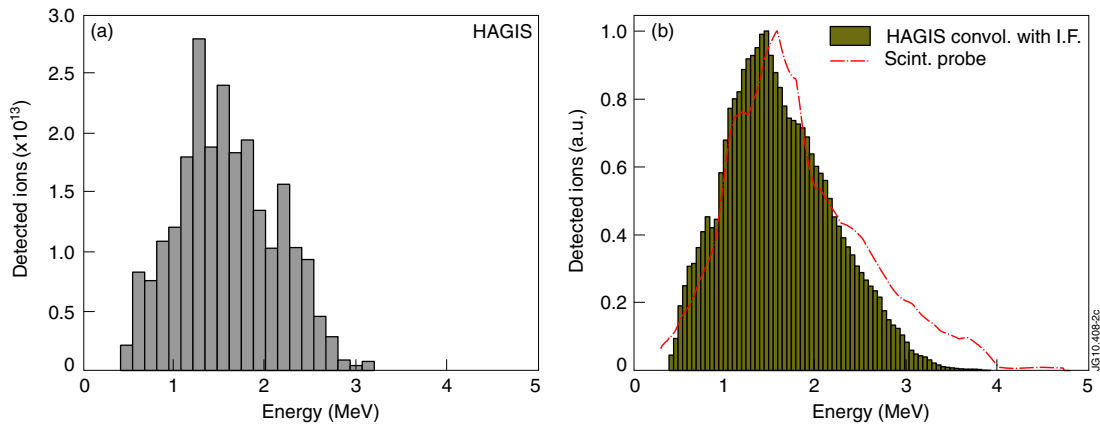

Figure 6. (*a*) Energy distribution of proton losses arriving at the scintillator, predicted by HAGIS for a fishbone with amplitude $A_{\rm sat} = 1.0 \times 10^{-2}$. (*b*) The same energy distribution convoluted with the instrumental function of the diagnostic, and energy distribution of losses measured by the scintillator probe diagnostic for the first fishbone shown in figure 5, for which a saturation amplitude value $A_{\rm sat} = 0.96 \times 10^{-2}$ (with 20–30% uncertainty) has been inferred from ECE measurements. The choices of width of the bars in (*a*) and (*b*) are arbitrary and not linked to each other.

where it is plotted together with the actual measurement for a fishbone of similar amplitude. It can be seen that the agreement between the two is striking, especially considering that several modelling steps had to be concatenated in order to arrive at this result. The simulated losses follow the measured curve closely almost over the entire energy range and peaks at the right values. Only at the highest energies (∼3 MeV) are the losses somewhat underestimated. (This indicates that the original SELFO distribution may have been

somewhat underestimating the number of ions contained in the high-energy tail.) Compared with the old simulation results, for which good agreement was only found if the core losses were artificially omitted, this constitutes a major improvement. The earlier results suggested that the core losses were being overestimated, but those have in fact not diminished in the new model. Hence, the improvement must come from the more accurate geometrical treatment of the losses selection.
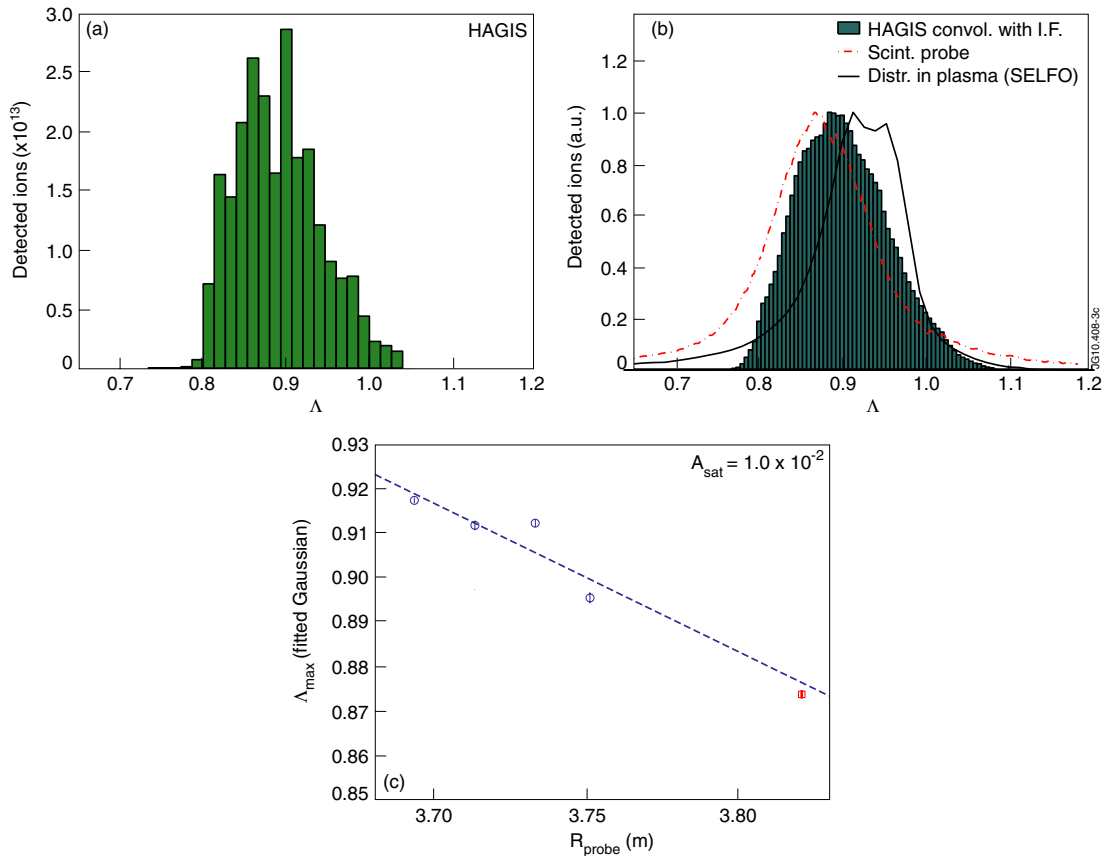
Figure 7. (*a*) Λ distribution of proton losses arriving at the scintillator, predicted by HAGIS for a fishbone with amplitude $A_{\rm sat} = 1.0 \times 10^{-2}$ and a synthetic diagnostic position $R = 3.751$ m. (*b*) The same Λ distribution convoluted with the instrumental function of the diagnostic, and the experimentally measured Λ distribution ($R = 3.821$ m) of losses for the same fishbone as in figure 6. Also shown is the Λ distribution of the total fast proton population inside the plasma. Note that all three distributions are here normalized to their respective maxima (only a tiny fraction of the original proton population in the plasma reaches the detector). The measured losses distribution (solid curve) peaks at $\Lambda = 0.874$, which corresponds to a pitch angle of 58.0°. A Gaussian fitted to the SELFO distribution (dotted curve) peaks at $\Lambda = 0.926$, which corresponds to a pitch angle of 61.0°. (*c*) Influence of the synthetic diagnostic radial position on the predicted Λ distribution. The *y*-axis denotes the Λ value at which a Gaussian function fitted to the losses has its maximum. The circles are for the simulations (HAGIS data convoluted with the instrumental function), whereas the square is the actual measurement (fitted Gaussian to the dashed–dotted curve in (*b*)). The error bars give the 95% confidence bounds of the fit only (other sources of error are not included). The linearly extrapolated value of the position of the Gaussian maximum predicted by the simulations for $R = 3.821$ m is in fairly good agreement (to within $\Lambda = 0.005$ or, equivalently, 0.25° in pitch angle) with the measurement.

The analogous comparison for the distribution of detected protons as a function of the pitch angle related orbit invariant Λ is shown in figures 7(*a*) and (*b*). Figure 7(*b*) includes in addition the initial SELFO distribution of protons in the plasma. Once more, the agreement between the measured and the detected losses distribution is excellent. Not only have the simulated losses the right shape (except for the regions far away from the maxima, where HAGIS underestimates the losses), but even the slight shift ($\Delta\Lambda \approx 0.08$) seen on the measured losses towards lower Λ values when comparing with the distribution inside the plasma can be reproduced. At this point, however, it is important to remember that the synthetic diagnostic position had been artificially shifted by a few cm towards the plasma. To assess the shift's impact, separate runs were performed in which the position of the probe was scanned radially, moving it further towards the plasma in small steps of about 2 cm. It turns out that while for the other results shown in this paper (e.g. the energy distribution) the probe position adjustments have a negligible effect on the predictions, for the pitch angle distribution it is not negligible.

What is observed is that the detected loss distribution remains Gaussian-like, but its shift with respect to the initial proton distribution varies. This is further illustrated in figure 7(*b*), where the position of the Gaussian peak is plotted against $R_{\rm probe}$. The trend is that the further outboard the probe is, the bigger the shift. Linearly extrapolating the simulation results to $R_{\rm probe} = 3.821$ m (which is the true position of the probe), we obtain an almost perfect match with the actually measured value (square). Overall, it is concluded that both for the energy and the pitch angle distributions, the simulations are in very good agreement with the experiment.

The experimental and the predicted time evolution of losses during a fishbone cycle are illustrated in figures 8(*a*) and (*b*), respectively. Experimentally, there is a fast initial rise of the scintillator signal until a peak is reached coinciding with the time when, or slightly after, the maximum fishbone magnetic perturbation amplitude occurs ($t = t_{\rm sat}$). Subsequently, the loss signal decays gradually. In figure 8(*b*), the light (yellow) bars represent the absolute number of protons arriving at the detector from HAGIS. Surprisingly (but actually
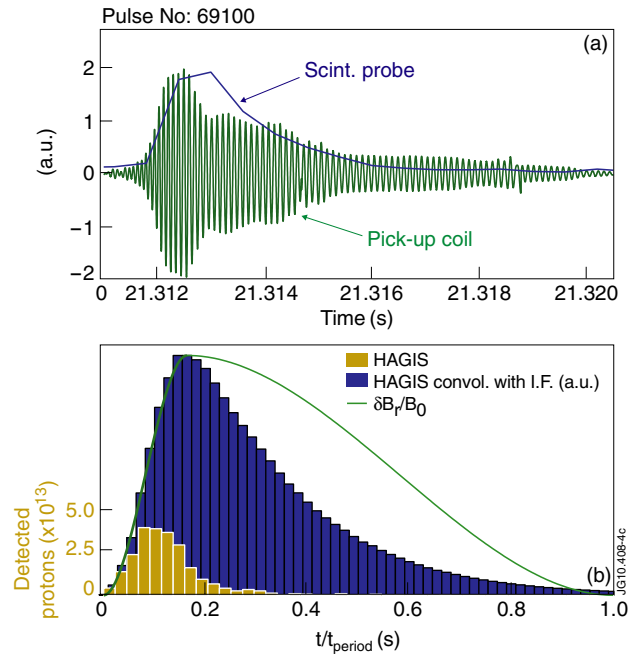
Figure 8. Detailed time evolution of losses for a single fishbone in discharge 69100. (*a*) Experimental behaviour: fast ion loss scintillator probe signal, overlaid with a magnetic fluctuation time trace from a pick-up coil. (*b*) Simulation result: number of protons arriving at the detector from HAGIS (light/yellow bars). It can be seen that almost all the protons arrive within the first 20% of the fishbone cycle and peak ahead of the magnetic perturbation amplitude. This feature is robustly observed in the simulations, not only for this particular fishbone but throughout the range of A_{sat} values relevant for this discharge. The solid bars show the same data folded with the time response of the diagnostic, and are in good qualitative agreement with the experimental loss signal in (*a*).

very similar to what was found in [10]), almost the entire losses take place prior to $t = t_{sat}$, and they peak at the time when the magnetic perturbation amplitude is only halfway to its saturation value (so, the losses stop increasing with amplitude). This *a priori* discrepancy with the experimental measurement disappears once the HAGIS prediction has been convoluted with the temporal response function of the scintillator material (see previous section), yielding the blue bars given in figure 8(*b*). It can be seen that the finite decay time of the scintillator material leads to a significant modification of the shape predicted by HAGIS, and in particular to a delay in the timing of the peak—which now basically coincides with the time of maximum perturbation amplitude—and a much longer tail. Overall, the synthetic trace is able to correctly reproduce the main features of the measured trace. The implication of this result is that, although our measurements initially suggested that the losses follow roughly the magnetic perturbation time trace, this is an instrument artefact. In reality the losses take place on a much faster time scale, roughly within the first ~20% of the fishbone cycle. At the moment the physical origin of the early loss maximum is unclear and will require further investigation (lack of fast ion refilling can be discarded, as discussed in [10]). Meanwhile, efforts are underway to install a new scintillator material inside the probe head (TG-Green, or $SrGa_2S_4 : Eu^{2+}$, previously used on ASDEX Upgrade [24, 25]), which has a much shorter phosphorescence time ($< 1\,\mu s$) and hence could provide confirmation of this

result. A comparison of measured and predicted proton losses per fishbone (i.e. integrated over the whole fishbone duration) as a function of the fishbone amplitude parameter A_{sat} is shown in figure 9. The experimental data in this plot were obtained from a sample of 26 fishbones in discharge 69100 ($t = 22.170$–$23.110\,s$), for which the obtained amplitudes range from 0.3×10^{-2} to 1.2×10^{-2}. A polynomial fit to the experimental data with linear and quadratic components yields essentially a purely quadratic increase in the losses with amplitude over the entire amplitude range. For the simulation data, a quadratic dependence of the losses is found as well at amplitudes $\delta \tilde{B}_{r,max}/B_0 \gtrsim 0.75 \times 10^{-2}$. However, for $\delta \tilde{B}_{r,max}/B_0 \lesssim 0.75 \times 10^{-2}$ the simulations predict a linear dependence (highlighted by the dashed–dotted line) which is not corroborated by the experiment. (Note that although the saturation effect described in figure 8 is still observed for each of the fishbones, the time-integrated losses do not saturate with amplitude. What happens is that the temporal shape of losses (light/yellow bars in figure 8) remains basically unchanged but the absolute losses scale up with the fishbone's A_{sat}.) Folding the HAGIS prediction with the instrumental function (not shown here) does not alter this trend, so the discrepancy is not due to an instrument artefact. The change from linear to quadratic losses with increasing mode amplitude can be understood in terms of a transition from near-boundary losses to stochastic (diffusive) losses, as described in [26] (see also [15, 27]), but keeping in mind that the wave–particle interaction is here non-resonant. The amplitude behaviour shown in figure 9(*a*) is essentially the same as that reported with the previous model [10]. (The only difference is that the absolute number of detected losses predicted by HAGIS has now increased by about a factor 4. For this comparison, however, the absolute level of losses is not meaningful as the scintillator diagnostic is not absolutely calibrated and hence a quantitative comparison is beyond our reach. Here we are only interested in the relative change with amplitude.) It has been argued in [10] that a mismatch between the simulated and the experimentally inferred values of A_{sat}, e.g. through neglecting the parallel plasma compressibility, is unlikely to be the cause of this discrepancy. Another possible source of discrepancy is variations in the fishbone duration, e.g. if small fishbones happen to be more shortlived than large ones (whereas in HAGIS the value of t_{period} was kept fixed at 11 ms). However, as shown in figure 9(*b*), there is only a very weak correlation (if any) between fishbone duration and amplitude, so this hypothesis can be ruled out as well.

4. Summary and conclusions

A model for the simulation of pitch angle and energy resolved fast ion loss measurements from a 2D scintillator probe has been presented and successfully tested against fishbones on JET. The improved geometrical description of scintillator probe measurements through the implementation of a synthetic diagnostic module in HAGIS—together with an accurate treatment of the diagnostic's instrumental function—has proven to be key to the correct reproduction of the two primary deliverables of the diagnostic, namely the energy and the pitch angle distribution of losses. Once folded with the finite time response of the diagnostic, good qualitative
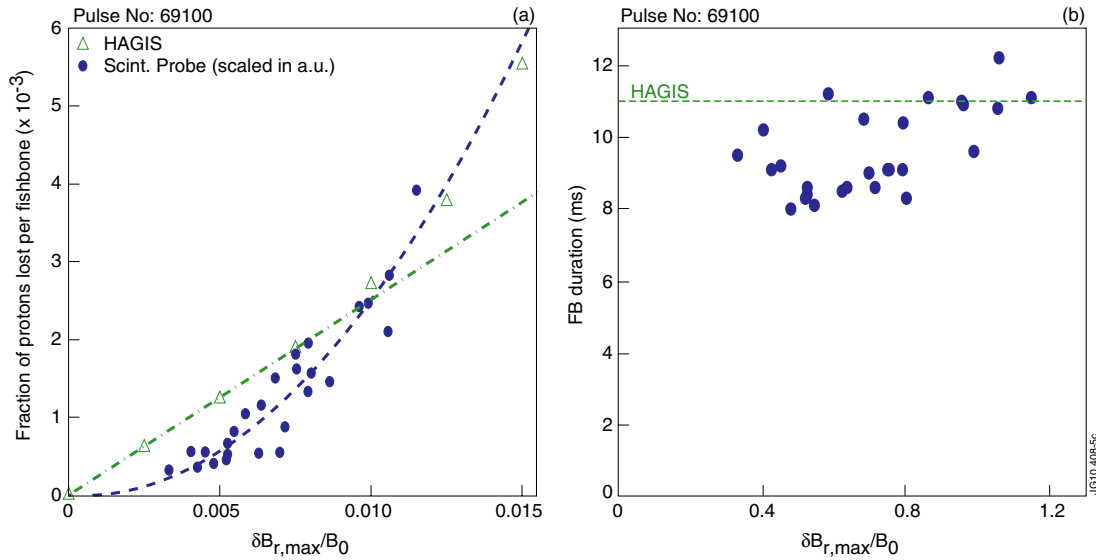
Figure 9. (*a*) Dependence of measured (circles) and simulated (triangles) losses (time-integrated over the entire fishbone) on the fishbone amplitude parameter $A_{sat} = \delta B_{r,max}/B_0$. For the experimental data, the value of A_{sat} has been obtained by matching the magnitude of magnetic flux surface displacements inside $q = 1$ (visualized through Poincaré plots of magnetic field lines in the 3D perturbed equilibrium) to electron temperature profile displacements at the time of maximum fishbone amplitude measured with an array of ECE radiometers. (*b*) Measured fishbone durations (inferred from a filtered magnetic fluctuation signal), and assumed value in HAGIS (dashed line). The dependence of the duration on the fishbone amplitude is very weak and hence cannot explain the differences in (*a*).

agreement between simulation and measurement is also found for the temporal behaviour of losses during a fishbone period. The simulations further suggest that nearly all the fast ion losses take place in the early growth phase of the fishbone cycle, and reach their maximum well ahead of the magnetic perturbation peak. Lacking an absolute calibration of the diagnostic, we have not attempted to compare the absolute number of losses, but at least their relative variation with the fishbone amplitude has been assessed, yielding more subtle differences between experiment and simulation for lower amplitude modes (i.e. quadratic versus linear increase with fishbone amplitude, respectively) which will require further investigation.

One of the limitations encountered (which could only be overcome through a small shift of the synthetic probe location towards the plasma boundary) was the inability to trace guiding centres beyond the separatrix. In the future, this could be overcome with the help of a recent extension to HAGIS by Bruedgam *et al* [28], which has been tested on ASDEX Upgrade but has still to be implemented for JET.

With only minor modifications this simulation technique can be applied to the study of other, more complex, instabilities, such as Alfvén eigenmodes or Alfvén cascades, against scintillator probe measurements. Dedicated JET experiments have been recently performed to study the influence of these instabilities on the fast ion confinement deterioration and loss [29], which are envisaged for future work.

Acknowledgments

References

[1] White R.B. *et al* 1995 *Phys. Plasmas* **2** 2871
[2] Heidbrink W.W. and Sadler G.J. 1994 *Nucl. Fusion* **34** 535
[3] Fasoli A. *et al* 2007 Progress in the ITER physics basis chapter 5: physics of energetic ions *Nucl. Fusion* **47** S264
[4] McGuire K. *et al* 1983 *Phys. Rev. Lett.* **50** 891
[5] Chen L., White R.B. and Rosenbluth M.N. 1984 *Phys. Rev. Lett.* **52** 1122
[6] Coppi B. and Porcelli F. 1988 *Fusion Technol.* **13** 447
[7] Heidbrink W.W., Hay R. and Strachan J.D. 1984 *Phys. Rev. Lett.* **53** 1905
[8] Duong H.H. and Heidbrink W.W. 1993 *Nucl. Fusion* **33** 211
[9] Zweben S.J. *et al* 1990 *Nucl. Fusion* **30** 1551
[10] Perez von Thun C. *et al* 2010 *Nucl. Fusion* **50** 084009
[11] Baeumel S. *et al* 2004 *Rev. Sci. Instrum.* **75** 3563
[12] Ödblom A., Breizman B.N., Sharapov S.E., Hender T.C. and Pastukhov V.P. 2002 *Phys. Plasmas* **9** 155
[13] Kadomtsev B.B. and Pogutse O.P. 1973 *Sov. Phys.—JETP* **39** 1012
[14] Strauss H.R. 1976 *Phys. Fluids* **19** 134
[15] Appel L.C. *et al* 1995 *Nucl. Fusion* **35** 1697
[16] Pinches S.D. *et al* 1998 *Comput. Phys. Commun.* **111** 133
[17] Yavorskij V.A., Darrow D., Goloborod'ko V.Ya., Reznik S.N., Holzmueller-Steinacker U., Gorelenkov N. and Schoepf K. 2002 *Nucl. Fusion* **42** 1210
[18] Reich M. *et al* 2006 Europhysics conference abstracts *Proc. 33rd EPS Conf. on Plasma Physics (Rome, Italy, 2006)* ed F. de Marco and G. Vlad (Geneva: EPS) vol 30 p 2.131 (cd-rom) http://epsppd.epfl.ch/Roma/pdf/P2_131.pdf
[19] Tuszewski M. and Zweben S.J. 1992 *Rev. Sci. Instrum.* **63** 4542
[20] Tuszewski M. and Zweben S.J. 1993 *Rev. Sci. Instrum.* **64** 2459
[21] Eriksson L.-G., Hellsten T. and Willén U. 1993 *Nucl. Fusion* **33** 1037

[22] Hedin J., Hellsten T., Eriksson L.-G. and Johnson T. 2002 *Nucl. Fusion* **42** 527

[23] Cheng C.Z. 1992 *Phys. Rep.* **211** 1

[24] García-Muñoz M. *et al* 2009 *Rev. Sci. Instrum.* **80** 053503

[25] García-Muñoz M. *et al* 2008 *Phys. Rev. Lett.* **100** 055005

[26] Hsu C.T. and Sigmar D.J. 1992 *Phys. Fluids* B **4** 1492

[27] García-Muñoz M. *et al* 2010 *Phys. Rev. Lett.* **104** 185002

[28] Bruedgam M. 2010 *PhD Thesis* Max-Planck Institut fuer Plasmaphysik, Garching, Germany

[29] Kiptily V.G. *et al* 2009 *Nucl. Fusion* **49** 065030